

Supporting Information

Managing the two mode outputs of triboelectric nanogenerators to reach a pulsed peak power density of 31 MW/m²

Junpeng Wu^{1†}, Xiaoyi Li^{1†*}, Na Xue¹, Jie Wang², Guoqiang Xu³, Shougang Chen¹, Hongzhi Cui^{1*}, Yunlong Zi^{4*}, Zhong Lin Wang^{2*},

1. College of Materials Science and Engineering, Ocean University of China, Qingdao 266100, China,

2. Beijing Institute of Nanoenergy and Nanosystems, Chinese Academy of Sciences, Beijing 101400, P. R. China

3. Department of Biomedical Engineering, The City University of Hong Kong, China

4. Thrust of Sustainable Energy and Environment, The Hong Kong University of Science and Technology (Guangzhou), Nansha, Guangzhou, Guangdong, 511400, China

† These authors contributed equally to this work.

*Corresponding author:

lixiaoyi@ouc.edu.cn; zlwang@binn.cas.cn; cuihongzhi@ouc.edu.cn; ylzi@ust.hk

Supplementary Text

Fig. S1. The three typical constant outputs modes: (a) a multiphase coupling mode, (b) a circuit design mode, and (c) energy management mode. These modes are tested to assess their outputs under conditions of discontinuous energy supply.

Fig. S2. The operational mechanism of the MC.

Fig. S3. Crest factor of current and voltage output of TENG-MC system at different loads.

Fig. S4. The (a) current, (b)voltage and (c)charge output signals of the TENG.

Fig. S5. Charging test of TENG-MC system at varying C_{in} .

Fig. S6. (a) Comparison of current signals with and without MC. (b) Power test of TENG. (c) Power test of TENG with MC.

Fig. S7. Comparison of studies on the peak power density of TENG

Fig. S8. The ultrahigh output mode of the TENG-MC system is able to power four individual 36W fluorescent lamps at a consistent operating frequency of 1Hz.

Fig. S9. The current of TENG-MC system for test with commercial multimeter.

Fig. S10. The time constant at different capacitances

Fig. S11. The conversion efficiencies of the TENG-MC system were calculated for different C_{in} capacitances at 60 s and 10 minutes intervals.

Fig. S12. Reveal the (a) breakdown current and (b) time intervals for varying intervals of the spark device, demonstrating the effect of spark device on the system's performance.

Fig. S13. The peak voltage of TENG-MC system in different distance.

Fig. S14. The peak current of TENG-MC system at varying C_{in} (from 0.78 nF to 47 nF).

Fig. S15. LL mode conversion efficiency at different loads and its fitted curves.

Fig. S16. Conversion efficiency of MC-LL mode at different inductances.

Fig. S17. Detailed calculations on the crest factor of TENG for the three

modes.

Fig. S18. Comparison of studies on the crest factor of TENG.

Fig. S19. The schematic of two TENG systems to test constant current capability.

Fig. S20. Brightness decay graph of 176LEDs.

Fig. S21. (a) Voltage graph of the TENG system and the TENG-MC system charging a 220nF capacitor. (b) After 2.5 minutes of operating time, the variation of current with time is plotted under different LEDs lit by the two systems respectively

Fig. S22. Effect of charging in MC-LL mode for 1.5 minutes to power 464 LEDs continuously. The effect of the remaining energy to power 232 LEDs without any further energy input.

Fig. S23. The detailed voltage comparison and grey scale statistics of 464 LED.

Fig. S24. The voltage outputs of TENG and TENG-MC systems under irregular discontinuous energy input.

Fig. S25. Detailed schematic of the corrosion test device.

Fig. S26. The steel sheets were test to three distinct conditions: (b) unprotected, (c) under continuous TENG system protection, and (a) under TENG-MC system.

Fig. S27. Corrosion protection effect of three systems on steel.

Fig. S28. Schematic diagram of destruction of worm eggs by strong electric current.

Fig. S29. Optical picture of larval tissue before and after strong current breakdown.

Fig. S30. Plot of UO mode damage to eggs in different environments (water or air).

Table S1 Insecticidal efficiency of UO mode.

Reference

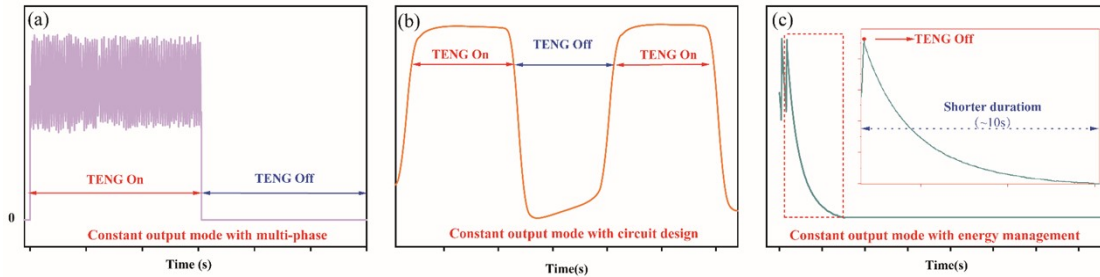


Figure S1. The three typical constant outputs modes: (a) a multiphase coupling mode, (b) a circuit design mode, and (c) energy management mode. These modes are tested to assess their outputs under conditions of discontinuous energy supply

As depicted in Figure S1a, this configuration allows the TENG to maintain a stable output within an acceptable range of fluctuation when in a steady state. However, it's noteworthy that the system's output plummets to zero the moment the TENG ceases operation. Circuit design is pivotal in securing a stabilized current output by orchestrating the interaction of electronic components within an external circuit. As illustrated in Figure S1b, such design improvements have bolstered the DC output stability, bringing the TENG's output closer to a consistent current during operation. However, the output still sharply falls to zero if the TENG stops operation, indicating that the system has not yet overcome the constraints associated with mechanical activation. Extensive research has revealed that energy management strategies can significantly enhance the energy output of TENGs, ensuring both stability and continuity in DC output. As demonstrated in Figure S1c, these strategies allow for a consistent energy output within a designated range. Importantly, the TENG can continue to deliver output for a limited time even after its operation has ceased.

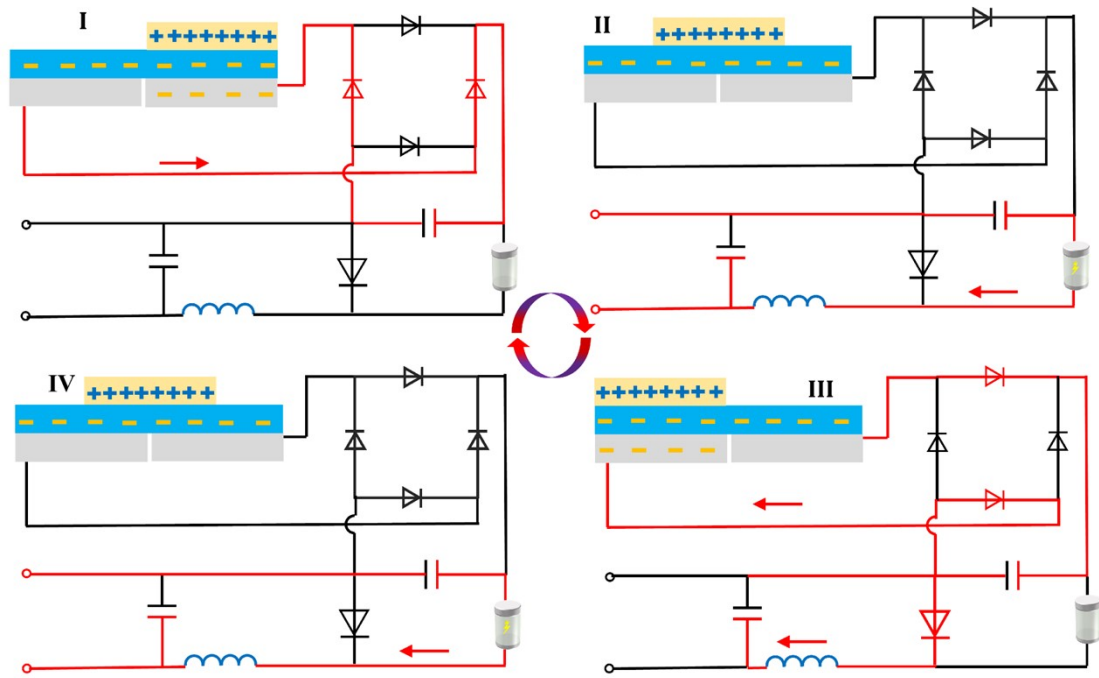


Figure S2. The operational mechanism of the MC.

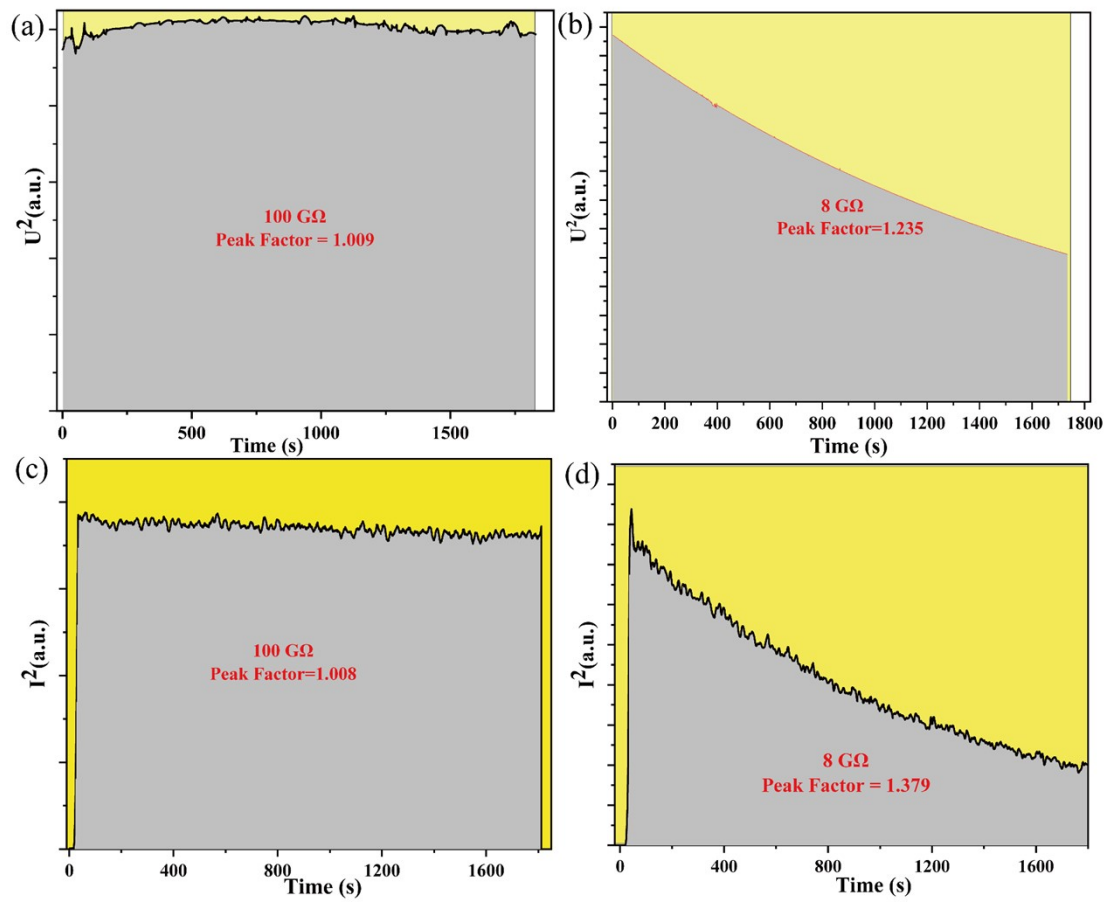


Figure S3. Crest factor of current and voltage output of TENG-MC system at different loads.

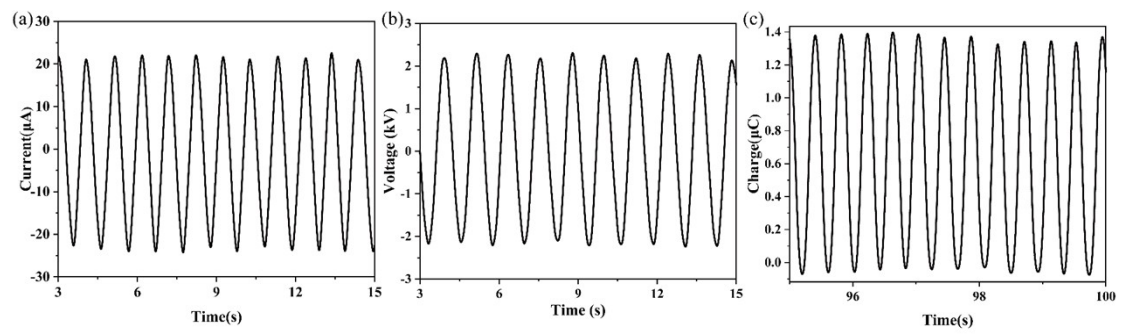


Figure S4. The (a) current, (b)voltage and (c)charge output signals of the TENG.

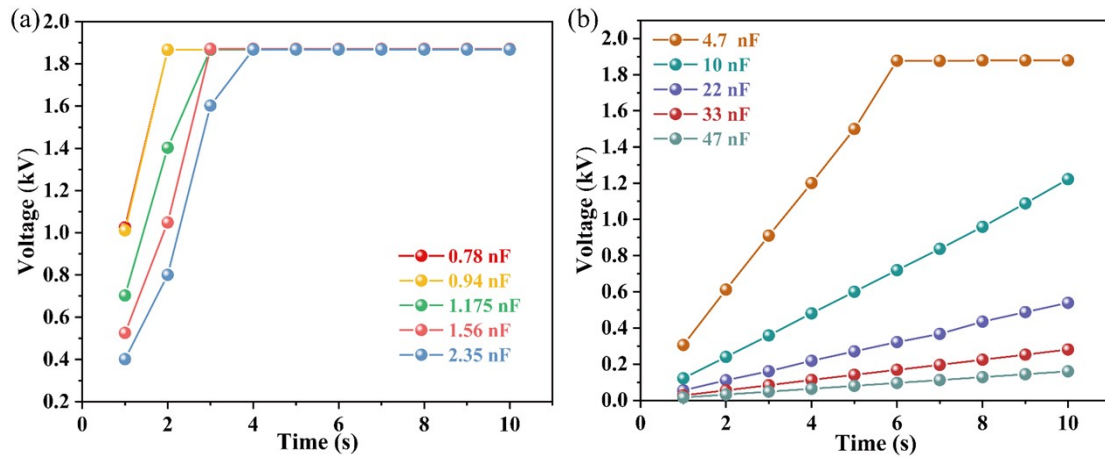


Figure S5. Charging test of TENG-MC system at varying C_{in} .

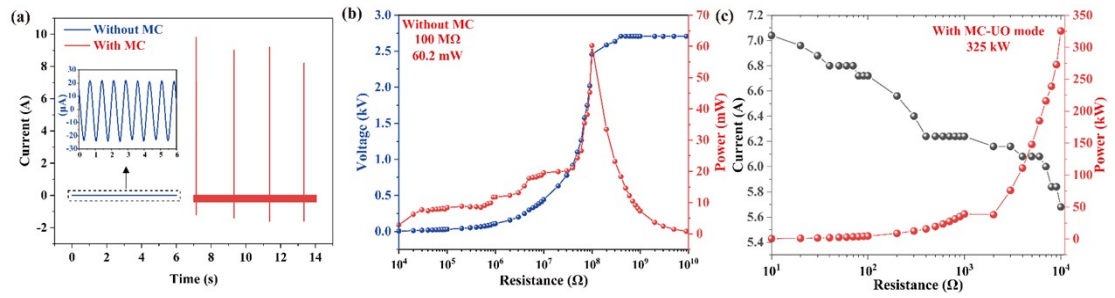


Figure S6. (a) Comparison of current signals with and without MC. (b) Power test of TENG. (c) Power test of TENG with MC.

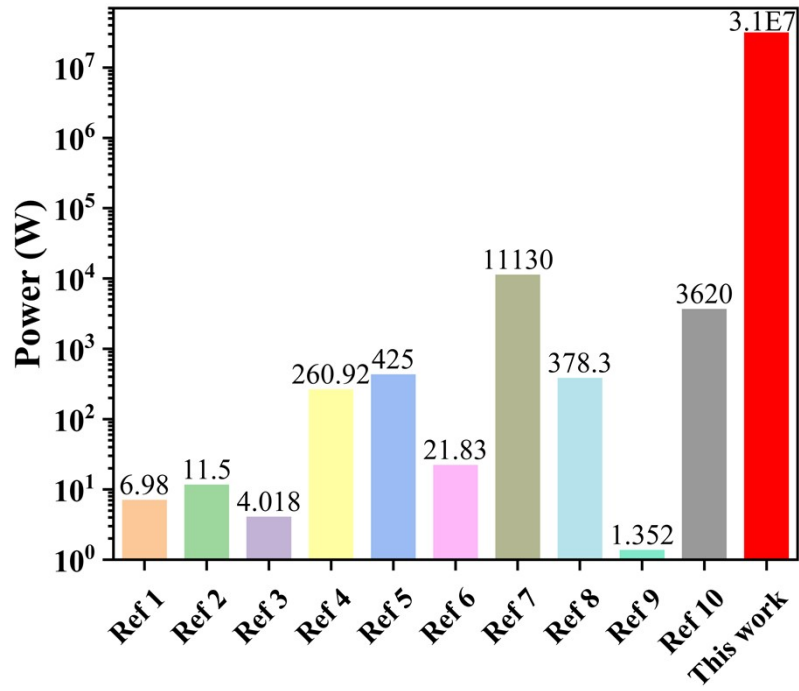


Figure S7. Comparison of studies on the peak power density of TENG [1-10].

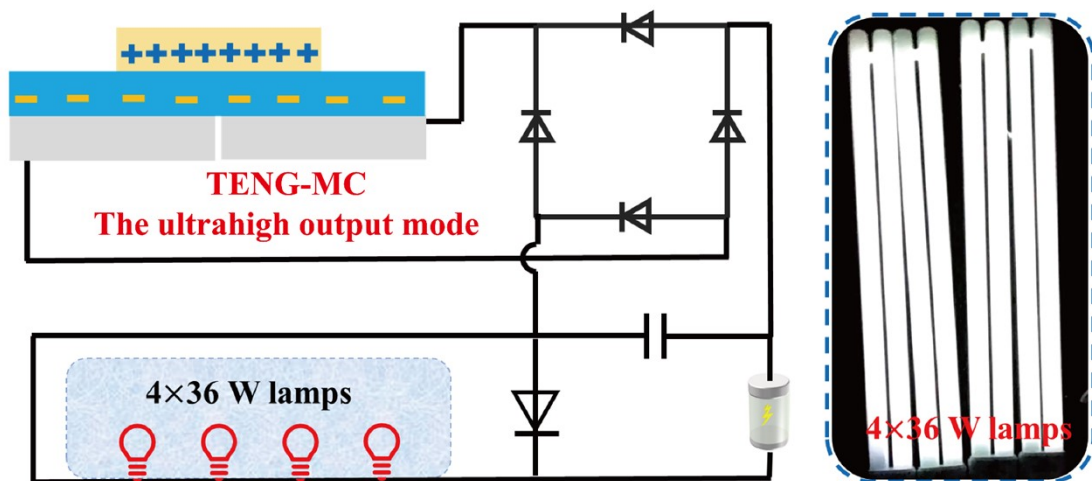


Figure S8. The ultrahigh output mode of the TENG-MC system is able to power four individual 36W fluorescent lamps at a consistent operating frequency of 1Hz.

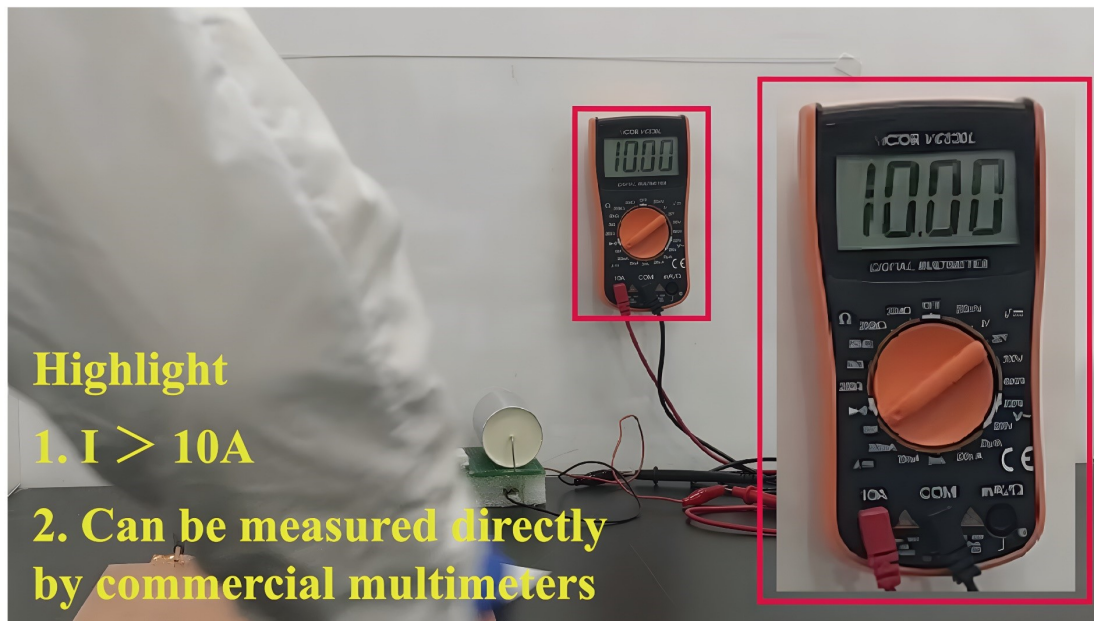


Figure S9. The current of TENG-MC system for test with commercial multimeter.

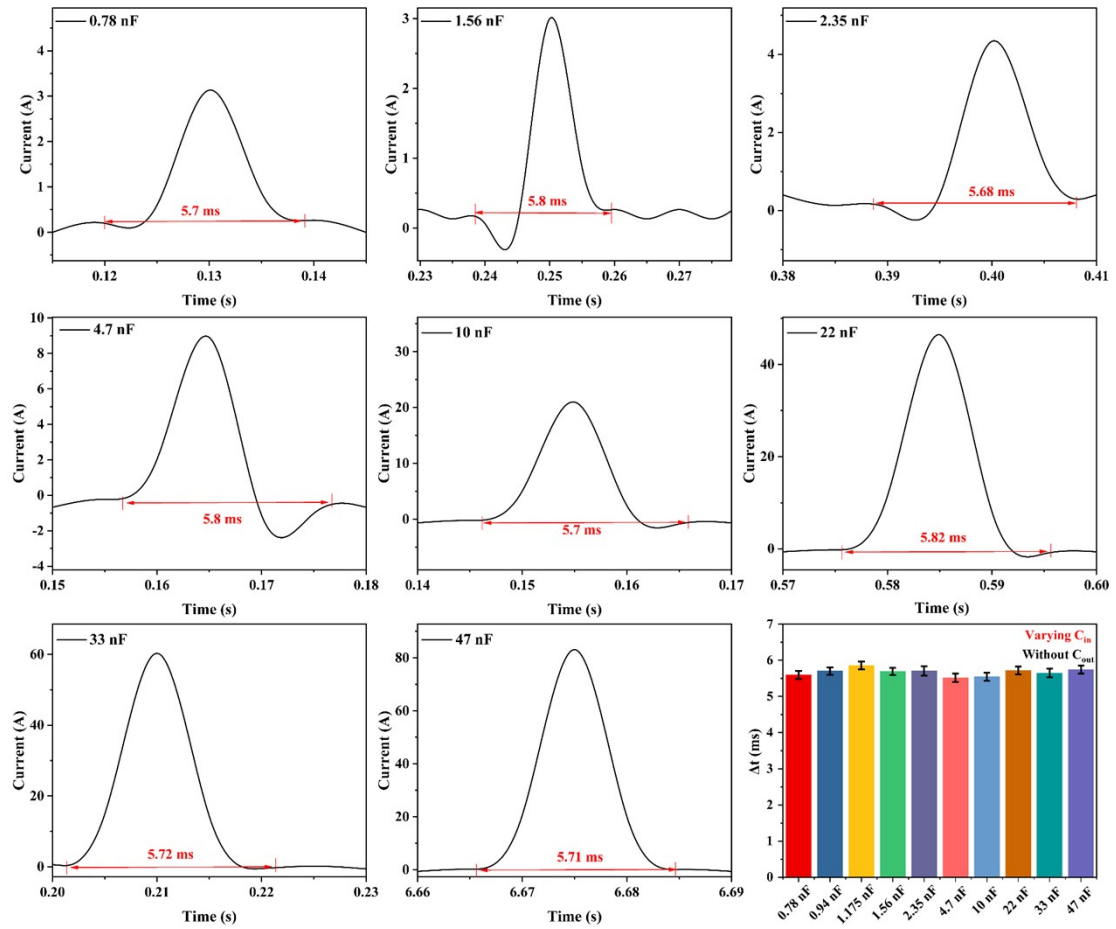


Figure S10. The time constant at different capacitances

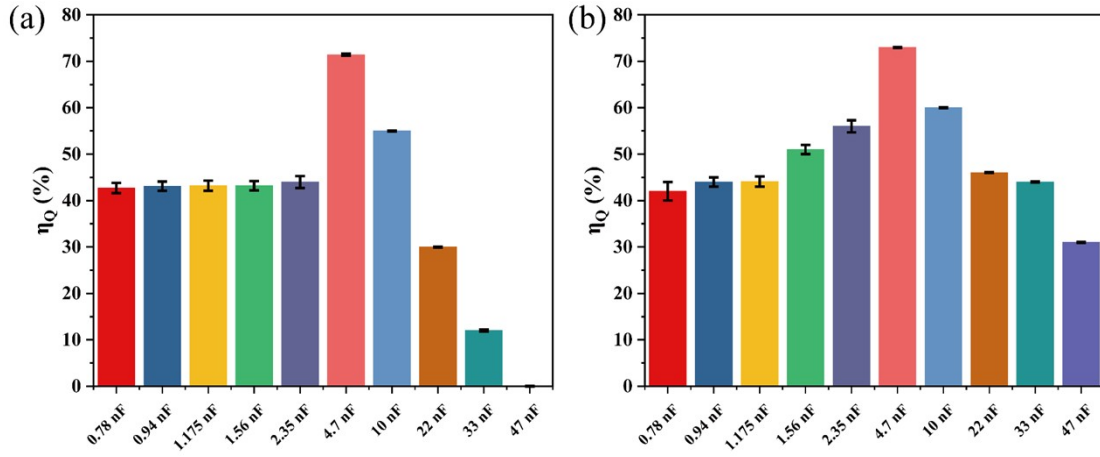


Figure S11. The charge storage efficiency of the TENG-MC system were calculated for different C_{in} capacitances at 60 s and 10 minutes intervals.

The formula for calculating the n :

$$n = \frac{T}{t_{TENG}} \quad (1)$$

In formula (1), T refers to the working time and t_{TENG} refers to the period of TENG.

$$Q_t = n \times Q_{TENG} \quad (2)$$

Q_t in equation 2 is the total charge during the operating time t . The value of Q_{TENG} is taken from Figure S4c. Where the transferred charge of the UO mode is calculated by equation 3:

$$Q_{Uo} = \int_0^t f(t) dt \quad (3)$$

$F(t)$ in equation 3 refers to the evolution of the current under different capacitances and the detailed data is shown in Figure S10.

The charge storage efficiency of UO under different capacitances is η_Q :

$$\eta_Q = \frac{Q_{Uo}}{Q_t} \quad (4)$$

The charge transfer efficiency under different times is obtained according to different values of T , respectively. In particular, it is worth noting that when C_{in} is 47

nf, no breakdown current is generated in 60s, so η_Q is 0.

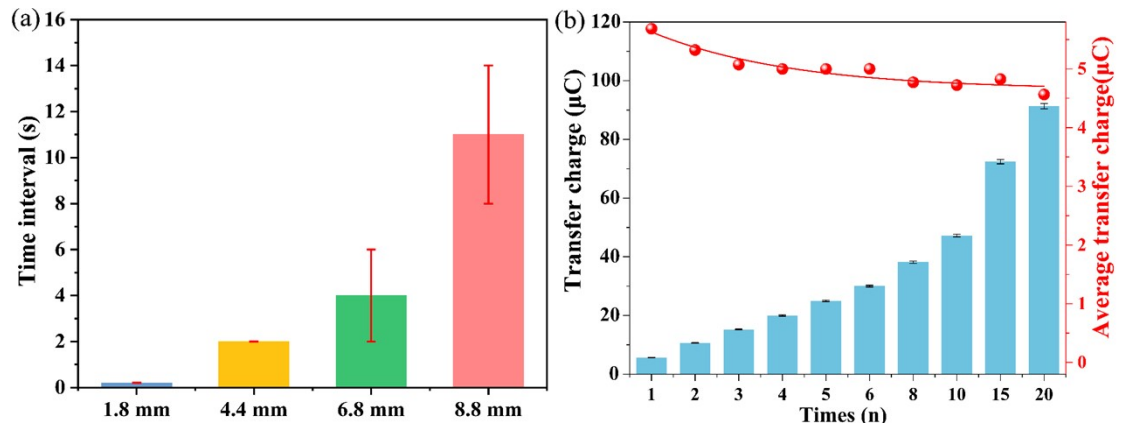


Figure S12. (a) Reveal the time intervals for varying gaps of the spark device, demonstrating the effect of spark device on the system's performance. (b) total charge transfer amount (histogram) and single transfer charge amount (line graph) under different breakdown counts of the spark device.

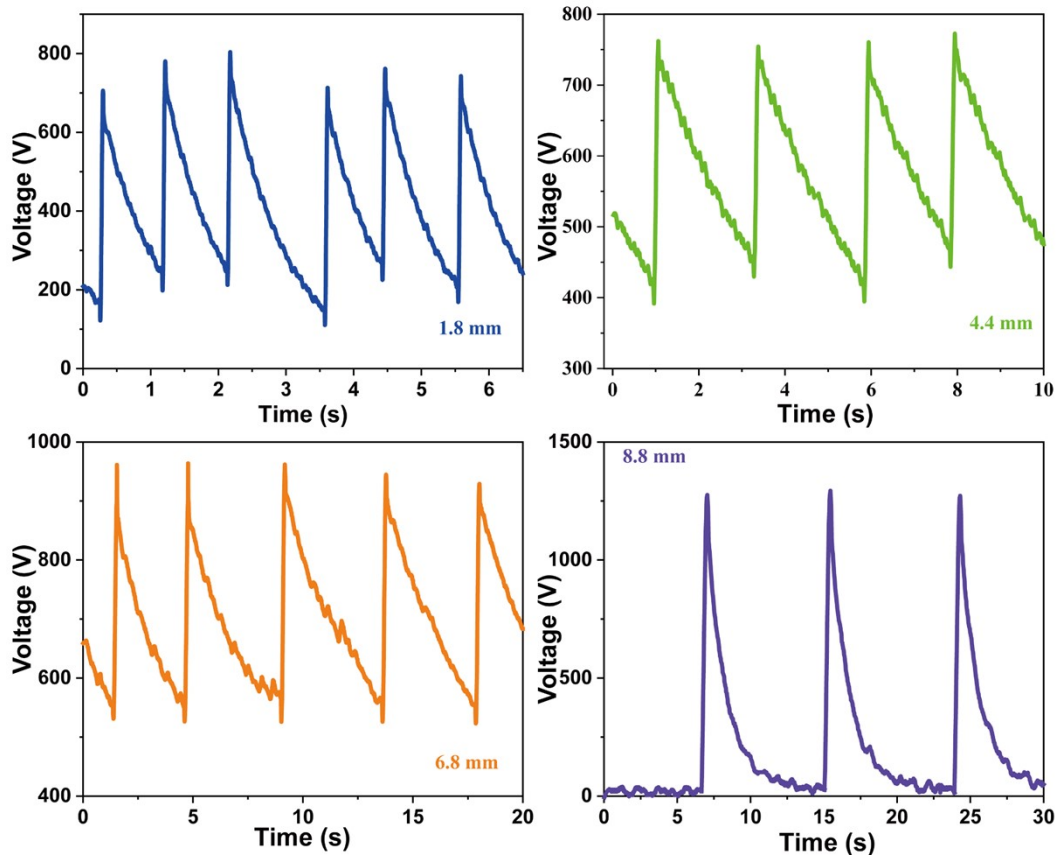


Figure S13. The peak voltage of TENG-MC system in different distance.

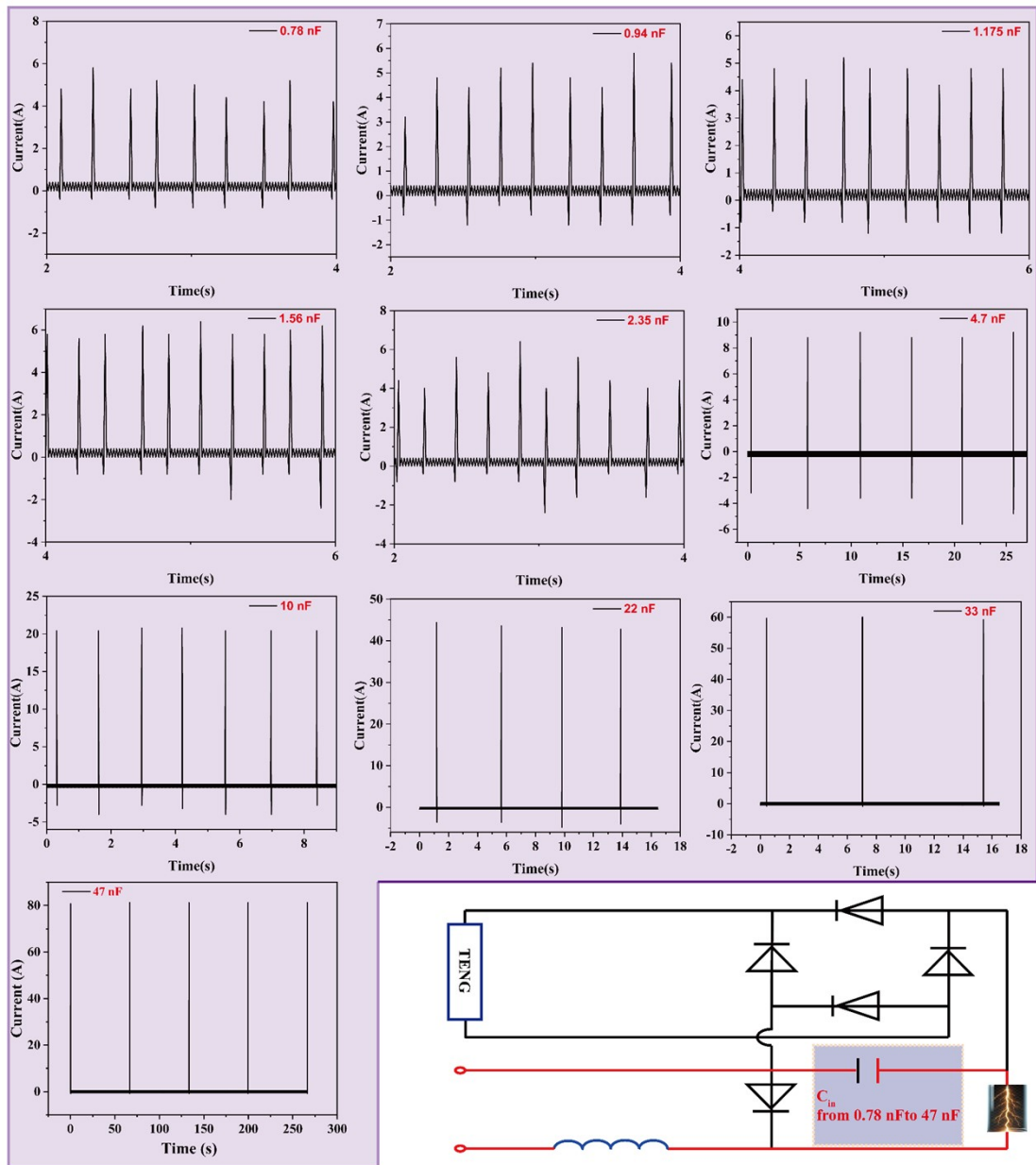


Figure S14. The peak current of TENG-MC system at varying C_{in} (from 0.78 nF to 47 nF).

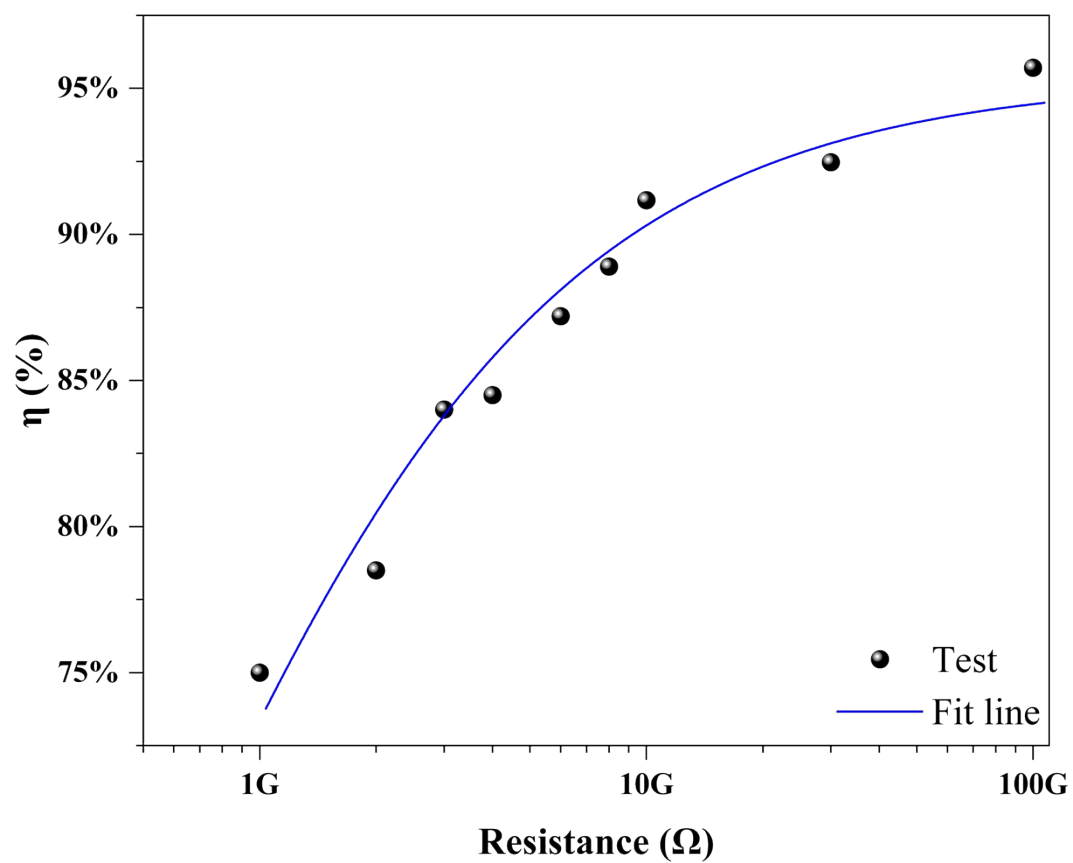


Figure S15. The conversion efficiency LL mode at different loads and its fitted curves.

The output energy in a half cycle (E) on load resistances ranging from 1 kΩ to 100 GΩ are shown in Figure S6. For a freestanding triboelectric-layer mode of TENG, the theoretical maximized E in cycle satisfies the equation:

The formula for calculating the E_{Total} :

$$E_{Total} = \int_0^t I(t)^2 dt \cdot R \quad (5)$$

The total input energy (E_{Total}) of the LL mode is obtained by integrating the square

of the current of the TENG ($\int_0^t I(t)^2 dt$) and the product of the resistance as shown in Equation 5.

$$E_{LL} = \int_0^t I_{n,(t)}^2 dt \cdot R_n \quad (6)$$

The n of I_n and R_n in Equation 6 represent loads of different sizes. W_{Total} and W_{LL} are handled in the same way as the product of the current integral and the load.

In formula (5), T refers to the working time and t_{TENG} refers to the period of TENG.

The energy efficiency of LL mode under different loads is η :

$$\eta = \frac{E_{LL}}{E_{Total}}$$

As shown in Figure S15, the energy conversion efficiency of the LL mode gradually stabilizes with increasing resistance. The fitted curves also support this point.

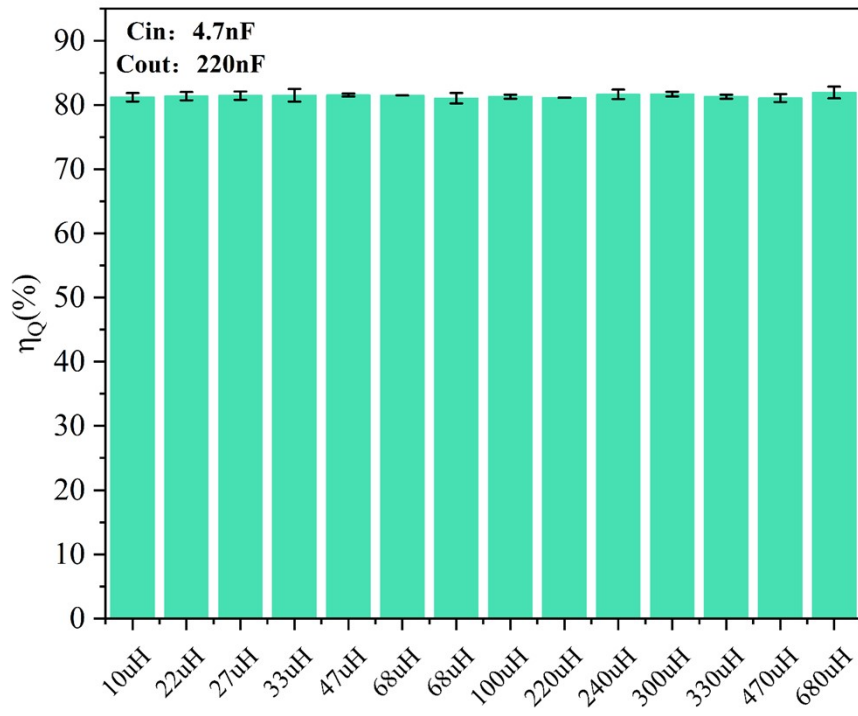


Figure S16. The charge storage efficiency of MC-LL mode at different inductances.

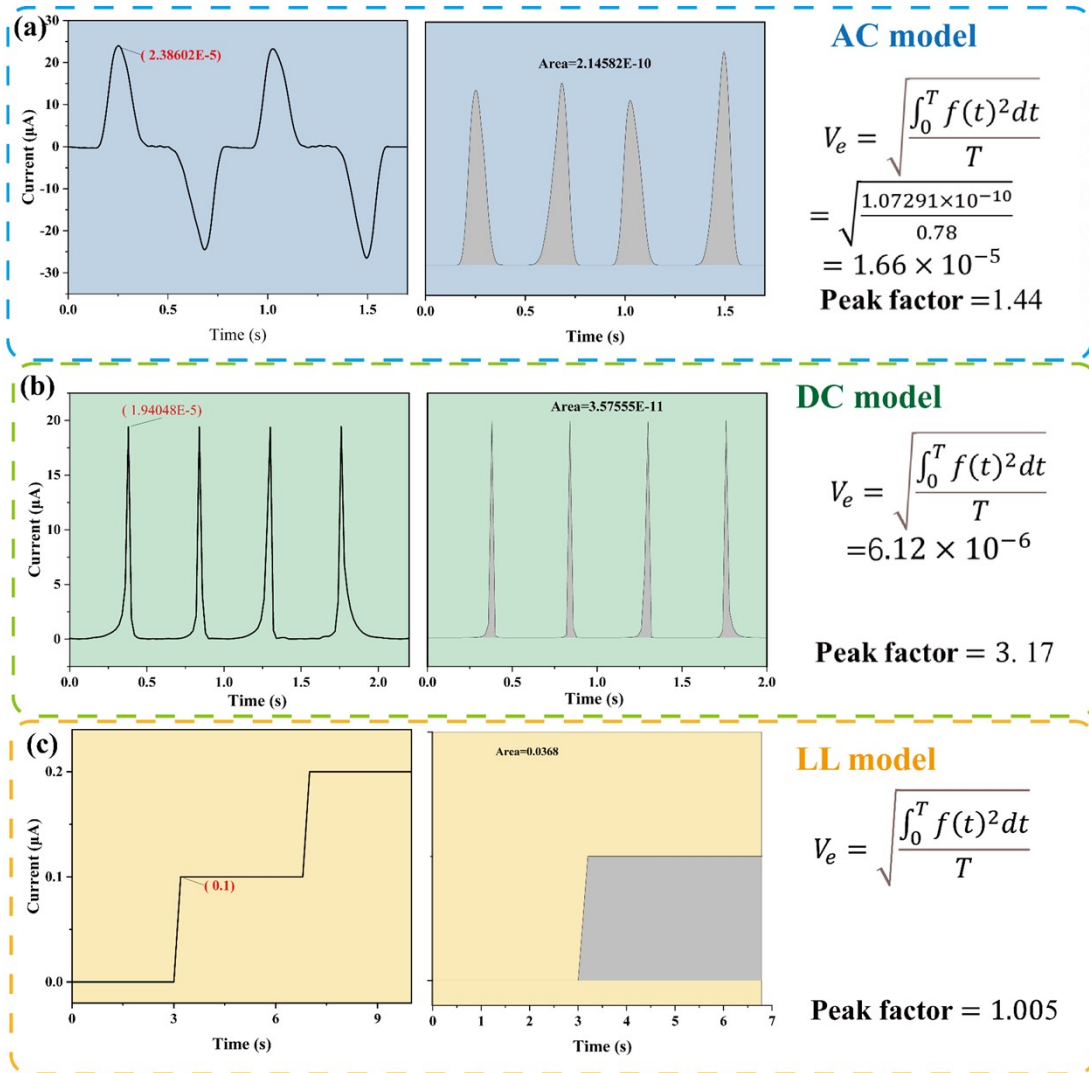


Figure S17. Detailed calculations on the crest factor of TENG for the three modes.

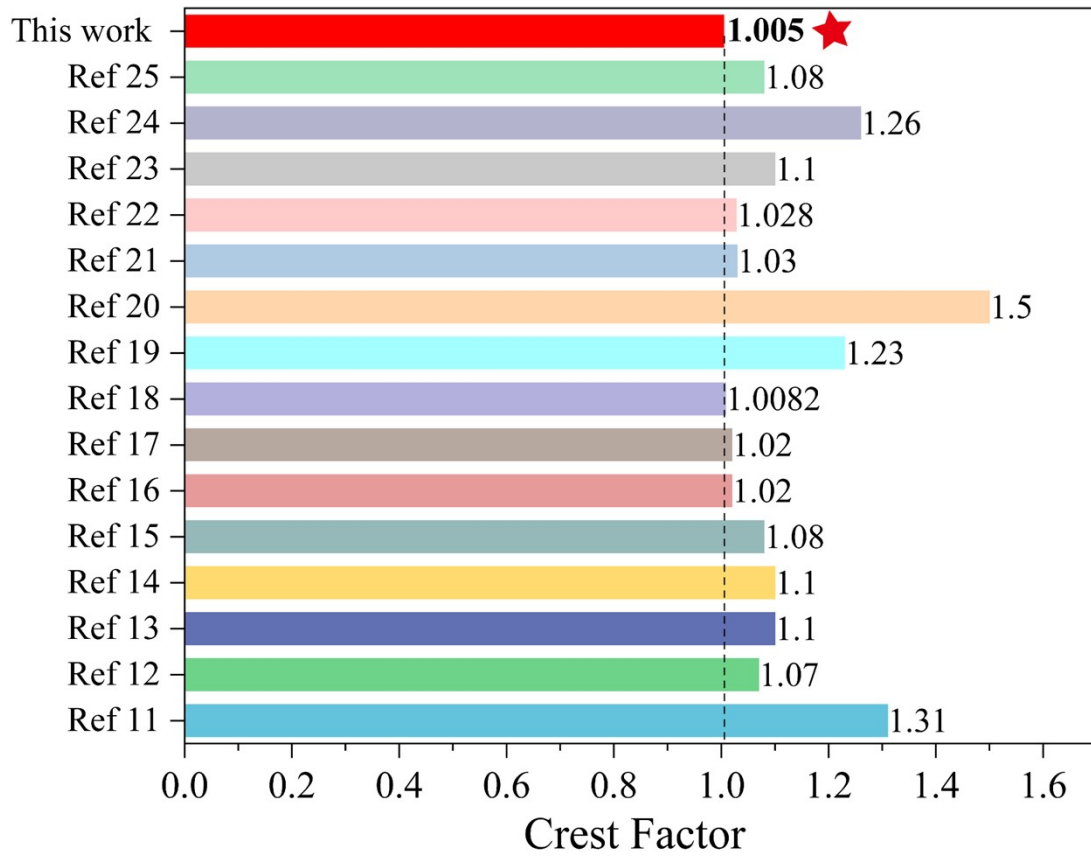


Figure S18. Comparison of studies on the crest factor of TENG.

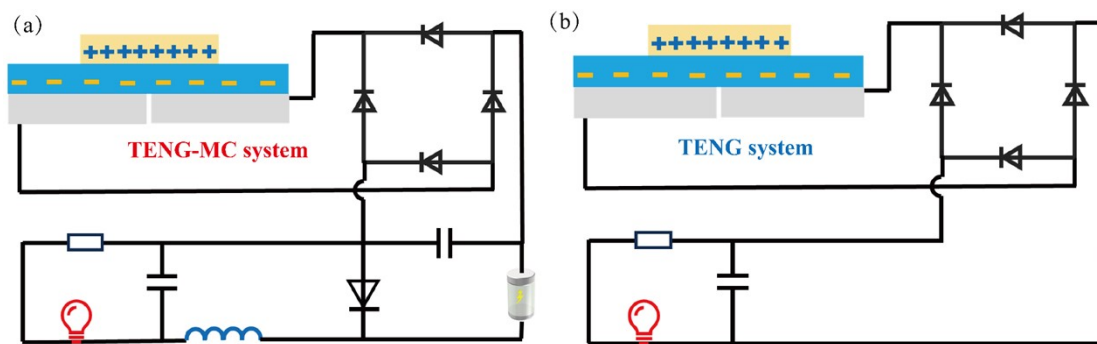


Figure S19. The schematic of two TENG systems to test constant current capability.

TENG system without MC LL mode

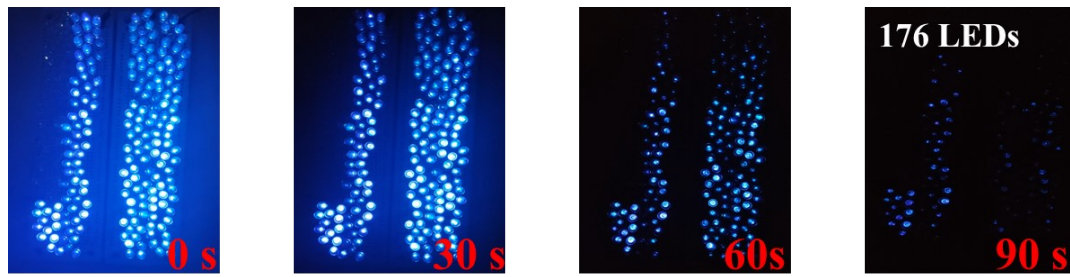


Figure S20. Brightness decay graph of 176LEDs.

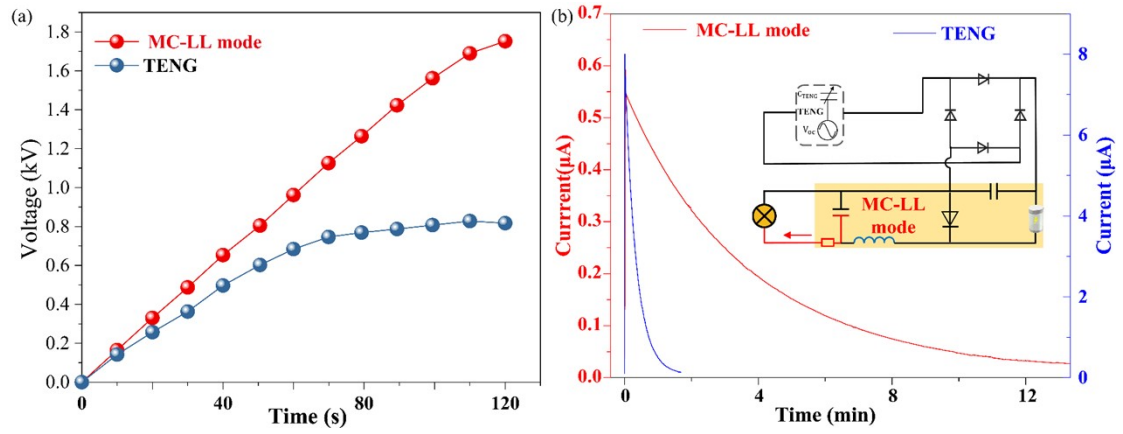


Figure S21. (a) Voltage graph of the TENG system and the TENG-MC system charging a 220nF capacitor. (b) After 2.5 minutes of operating time, the variation of current with time is plotted under different LEDs lit by the two systems respectively.

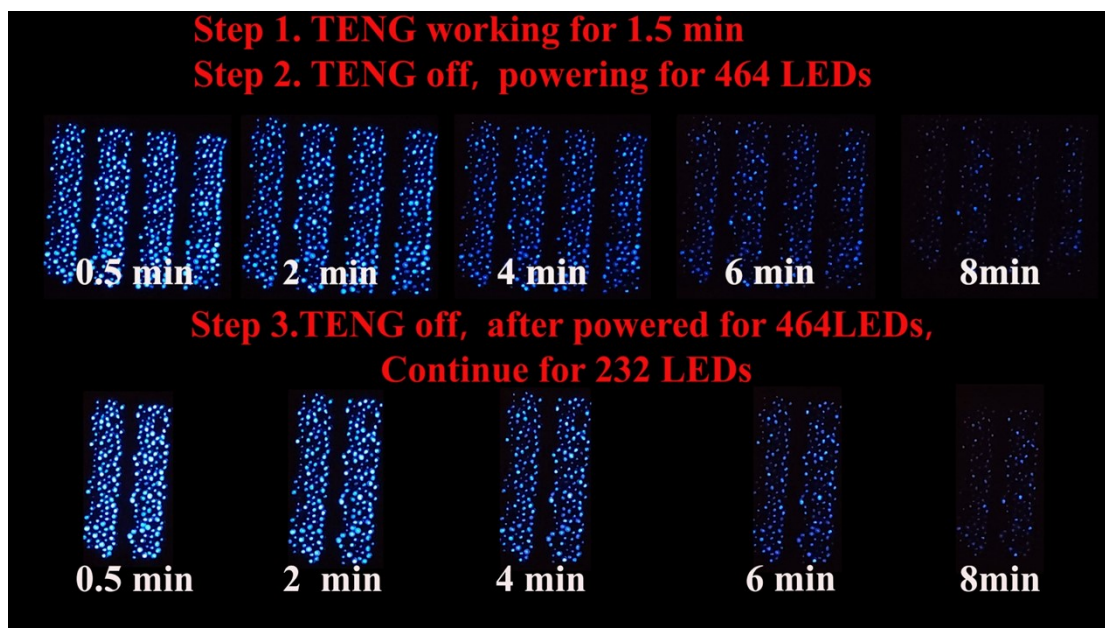


Figure S22. Effect of charging in MC-LL mode for 1.5 minutes to power 464 LEDs continuously. The effect of the remaining energy to power 232 LEDs without any further energy input.

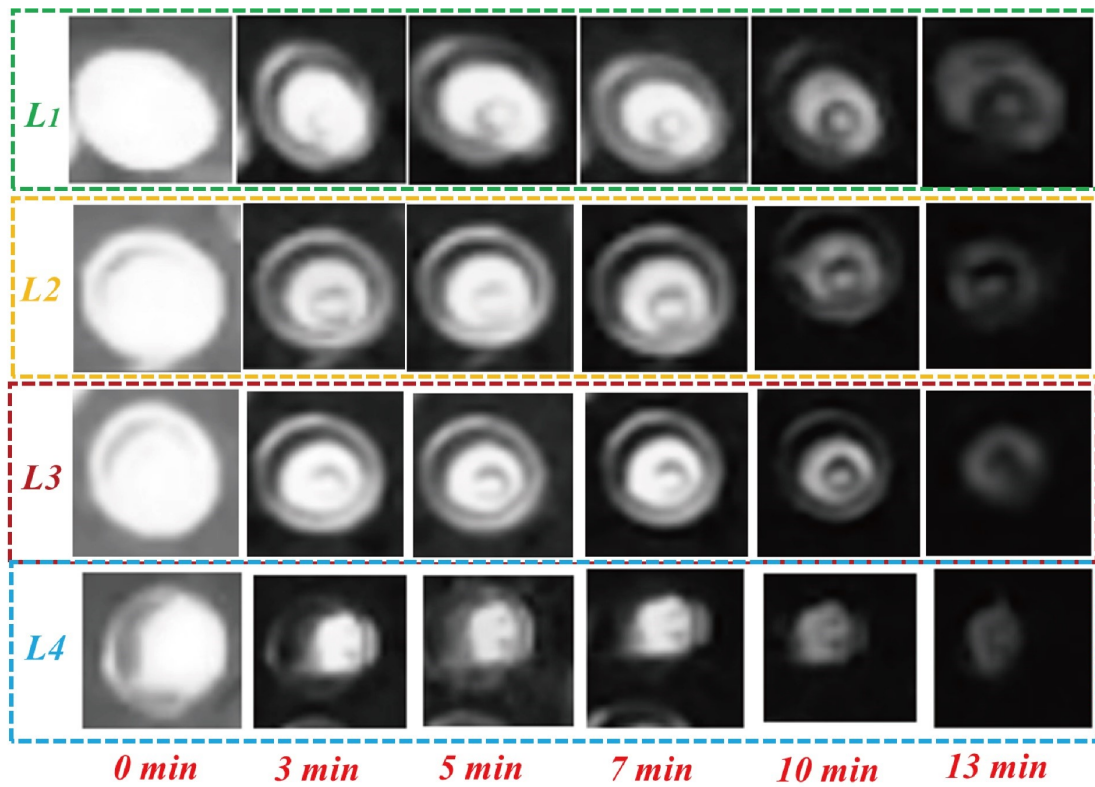


Figure S23. The detailed voltage comparison and grey scale statistics of LED.

The specific code of MATLAB :

```
% close all
```

```
% clear all
```

```
% clc
```

```
I = im2double(rgb2gray(imread('image.jpg')));
```

```
figure; imshow(I);
```

```
[mraw, ncol] = size(I);
```

```
Image AverageGray = sum(sum(I))/(mraw*ncol)
```

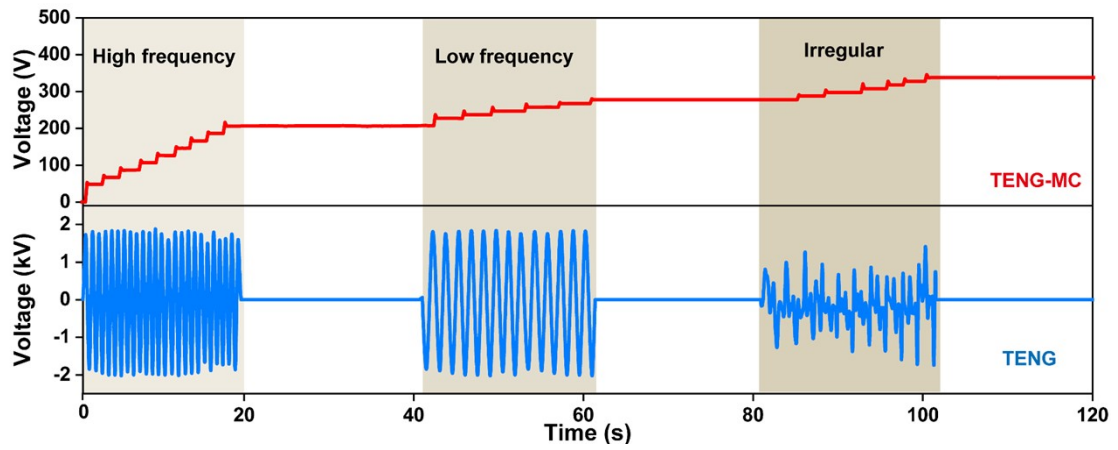


Figure S24. The voltage outputs of TENG and TENG-MC systems under irregular discontinuous energy input.

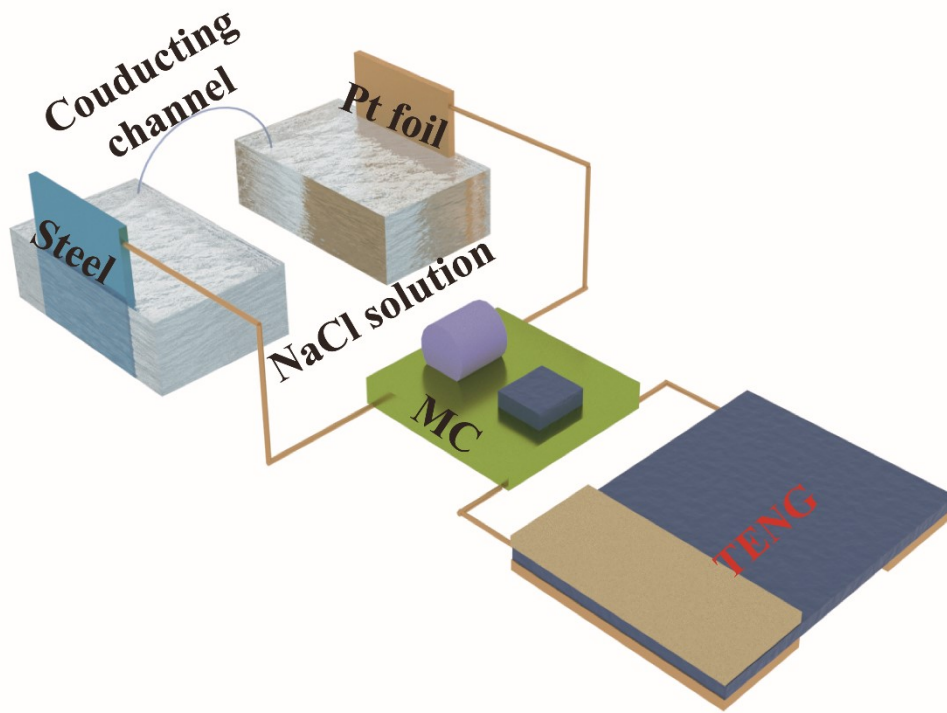


Figure S25. Detailed schematic of the corrosion test device.

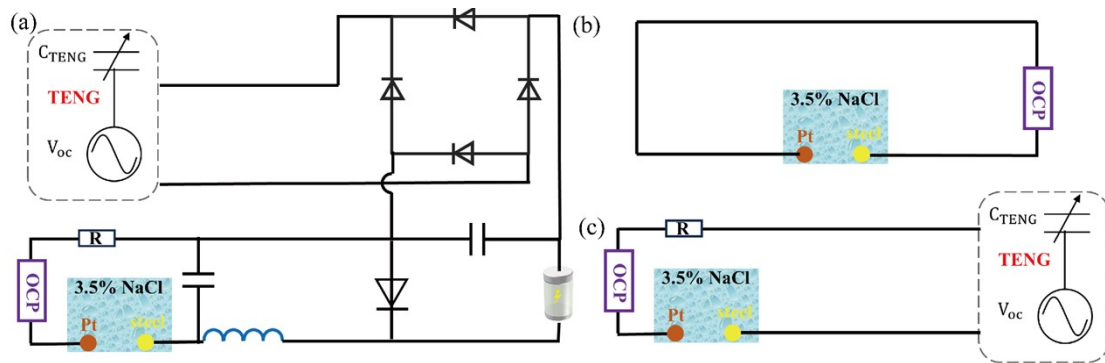


Figure S26. The steel sheets were test to three distinct conditions: (b) unprotected, (c) under continuous TENG system protection, and (a) under TENG-MC system.

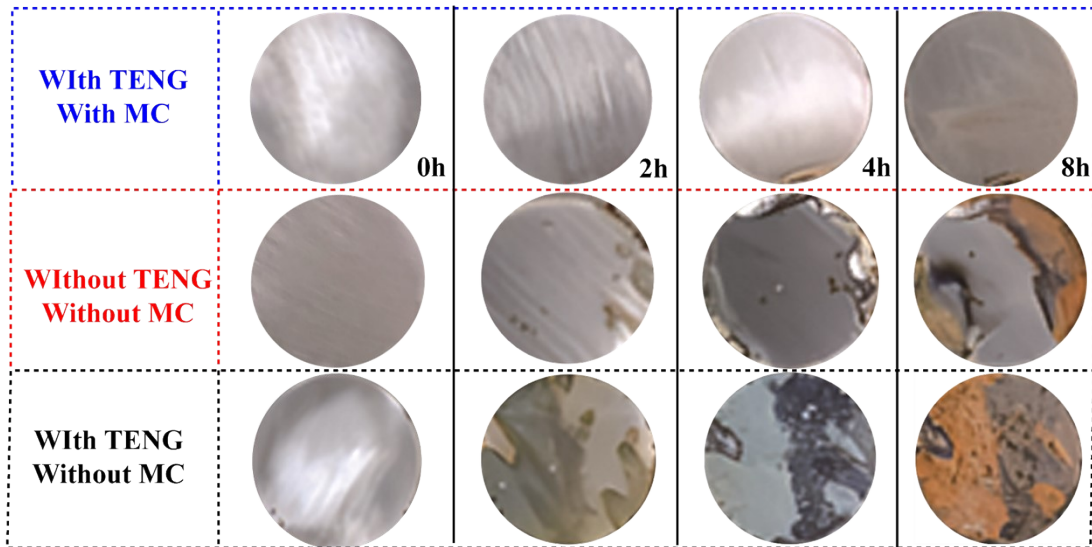


Figure S27. Corrosion protection effect of three systems on steel.

To accurately simulate a marine environment, we prepared a 3.5% sodium chloride solution. The corrosion test setup, illustrated in Figure S25, employed Q235-type steel plates as test electrodes and platinum electrodes as reference electrodes. The open circuit potential (OCP), as measured by the electrochemical workstation, serves to evaluate the effectiveness of the cathodic protection method when a current is applied. Upon halting the TENG-MC system after 2.5 minutes of operation, the OCP reached 710 mV, and remained stable at 674 mV for the ensuing 30 minutes, showcasing its high stability.

For a more direct demonstration of the TENG-MC system's corrosion protection capabilities, we conducted steel corrosion experiments. Initially, the steel sheet's surface was polished before immersion in the 3.5% NaCl solution alongside the platinum electrode. The steel sheets were subjected to three distinct conditions: unprotected, under continuous TENG system protection, and under TENG-MC system protection (with TENG ceasing after 2.5 minutes). Detailed information on this setup is available in Figure S26. We monitored the steel's corrosion progression in real-time, with the results displayed in Figure S27. The TENG-only system began exhibiting corrosion after 2 hours, with metal deterioration intensifying after 4 hours and complete corrosion with rust formation by 8 hours. The unprotected group showed no initial corrosion at 2 hours, significant edge corrosion at 4 hours, and partial surface corrosion with rust at 8 hours. Notably, the TENG-MC system demonstrated no change in the metal surface at 2 hours, pitting corrosion at the edges by 4 hours, and minimal surface corrosion without rust at 8 hours.

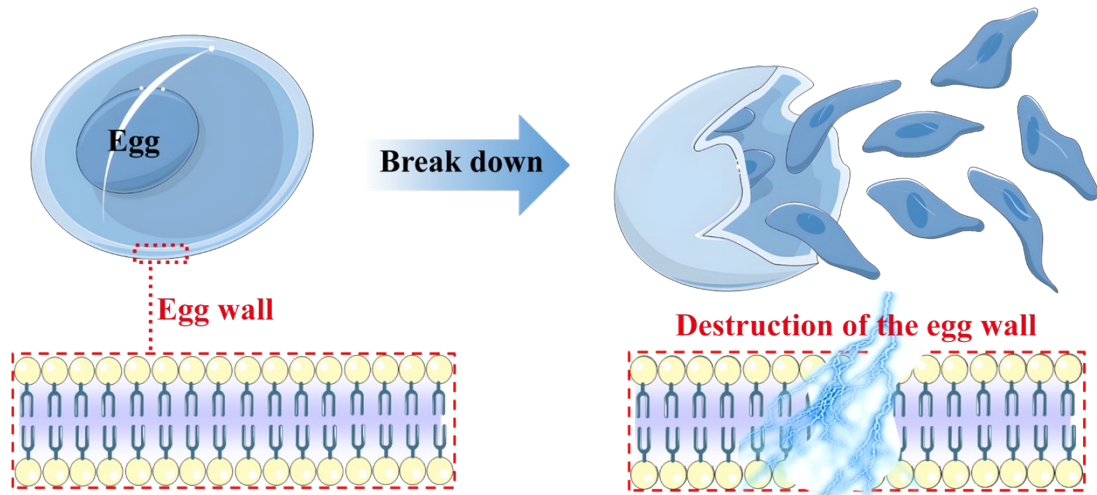


Figure S28. Schematic diagram of destruction of worm eggs by strong electric current.

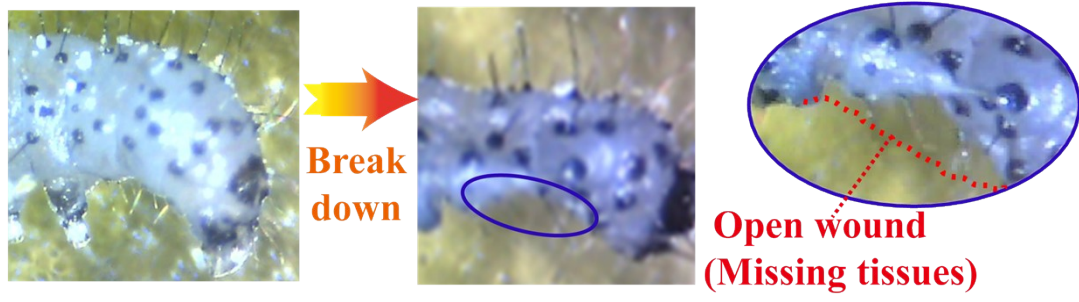


Figure S29. Optical picture of larval tissue before and after strong current breakdown.

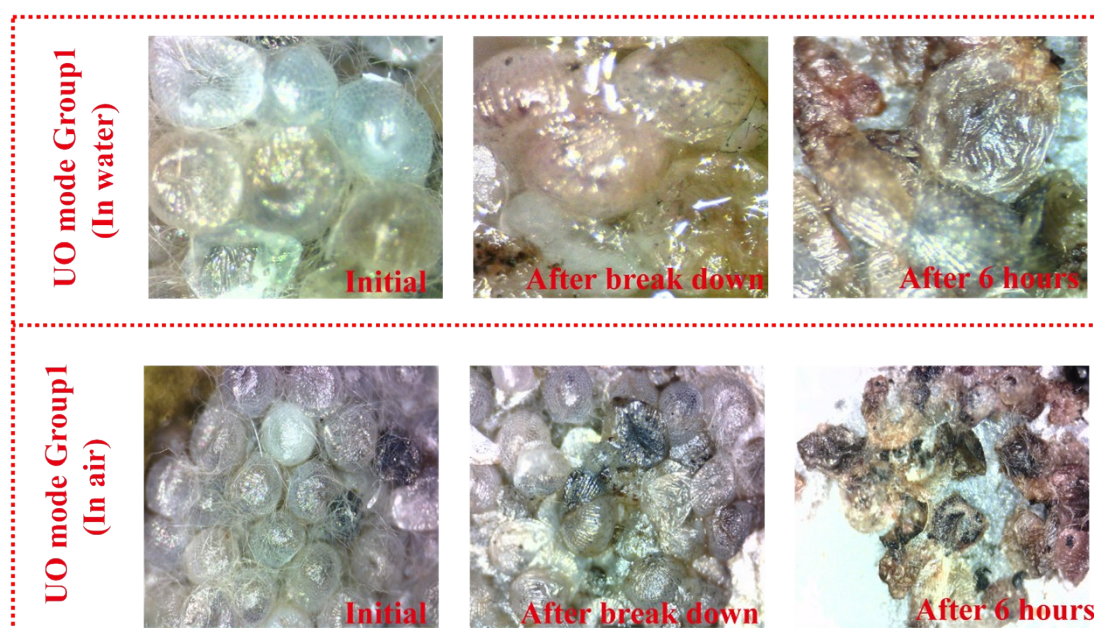


Figure S30. Plot of UO mode damage to eggs in different environments (water or air).

Table S1 Insecticidal efficiency of UO mode

	Total number of insect eggs	Number of killed eggs	Number of surviving eggs	Insecticide rate
Group 1	7	7	0	100%
Group 2	23	23	0	100%
Group 3	17	17	0	100%
Group 4	18	18	0	100%
Group 5	37	36	1	99.80%

Based on the UO mode of the pest control system, we conducted experiments to address various complex environments and better match actual applications. We tested pest extermination in both air and water environments. As shown in Figure S26, the initially selected insect eggs were smooth-surfaced and brightly colored. However, after the UO mode discharge, both in air and water, the egg walls were torn to varying degrees, and the contents flowed out, as shown in Figure S24. The eggs were all inactive and dried up within 6 hours. To verify the effectiveness of the UO-mode pest control system, several extermination experiments were conducted. The results, shown in Table S1, indicate a high insecticidal efficiency of over 99.8%

Reference

1. X. Li, X. Yin, Z. Zhao, L. Zhou, D. Liu, C. Zhang, C. Zhang, W. Zhang, S. Li and J. Wang, *Advanced Energy Materials*, 2020, 10, 1903024.
2. Y. Hu, X. Li, Z. Zhao, C. Zhang, L. Zhou, Y. Li, Y. Liu, J. Wang and Z. L. Wang, *Small methods*, 2021, 5, 2100936.
3. H. Luo, X. Ni, C. Zhang, Y. Cui, T. Yang, J. Shao and X. Jing, *Small*, 2024, 2406091.
4. P. Chen, J. An, R. Cheng, S. Shu, A. Berbille, T. Jiang and Z. L. Wang, *Energy & Environmental Science*, 2021, 14, 4523-4532.
5. J. Wang, Y. Li, Z. Xie, Y. Xu, J. Zhou, T. Cheng, H. Zhao and Z. L. Wang, *Advanced Energy Materials*, 2020, 10, 1904227.
6. C. Shan, K. Li, H. Wu, S. Fu, A. Liu, J. Wang, X. Zhang, B. Liu, X. Wang and C. Hu, *Advanced Functional Materials*, 2024, 34, 2310332.
7. K. Li, C. Shan, S. Fu, H. Wu, W. He, J. Wang, G. Li, Q. Mu, S. Du and Q. Zhao, *Energy & Environmental Science*, 2024, 17, 580-590.
8. Q. Li, Y. Hu, Q. Yang, X. Li, X. Zhang, H. Yang, P. Ji, Y. Xi and Z. L. Wang, *Advanced Energy Materials*, 2023, 13, 2202921.
9. J. Wang, H. Li, D. Zhao, Q. Gao, X. Cheng, J. Wen, Z. L. Wang and T. Cheng, *Advanced Materials Technologies*, 2023, 8, 2300480.
10. N. Liu, D. Liu, Y. Gao, S. Li, L. Zhou, Z. Zhao, S. Cui, L. Liu, Z. L. Wang and J. Wang, *Small Methods*, 2022, 6, 2200066.
11. X. Li, C. Zhang, Y. Gao, Z. Zhao, Y. Hu, O. Yang, L. Liu, L. Zhou, J. Wang and Z. L. Wang, *Energy & Environmental Science*, 2022, 15, 1334-1345.
12. P. Liu, T. Zhong, G. Xu, W. Mao, S. Yang, Z. Jiang, C. Xu and Q. Song, *Applied Energy*, 2024, 367, 123400.
13. R. Zhang, H. Lin, Y. Pan, C. Li, Z. Yang, J. Tian and H. C. Shum, *Advanced Functional Materials*, 2022, 32, 2208393.
14. H. Ryu, J. H. Lee, U. Khan, S. S. Kwak, R. Hinchet and S.-W. Kim, *Energy & Environmental Science*, 2018, 11, 2057-2063.

15. H. J. Hwang, D. Kwon, H. Y. Kwon, M. Shim, J. M. Baik and D. Choi, *Advanced Energy Materials*, 2024, 2400481.
16. X. Liu, K. Zhao and Y. Yang, *Nano Energy*, 2018, 53, 622-629.
17. D. Heo, J.-h. Son, H. Yong, J. Hur, K. Cha, S. Kim, M. Choi, J. Hong and S. Lee, *Nano Energy*, 2023, 116.
18. Q. Tang, M.-H. Yeh, G. Liu, S. Li, J. Chen, Y. Bai, L. Feng, M. Lai, K.-C. Ho, H. Guo and C. Hu, *Nano Energy*, 2018, 47, 74-80.
19. D. Heo, J. h. Son, D. Kim, M. Song, H. Ryu, S. Kim, K. Choi, Z. H. Lin, D. Kim, J. Hong and S. Lee, *Advanced Energy Materials*, 2023, 13.
20. J. H. Son, S. H. Chung, K. Cha, S. Kim, Z. H. Lin, J. Hong, J. Chung and S. Lee, *Adv Mater*, 2023, 35, e2300283.
21. S.-H. Chung, K. Cha, M. Song, D. Kim, D. Heo, M.-K. Kim, H. Jung, Y. Jin, J. Hong, J. Chung and S. Lee, *Nano Energy*, 2022, 103.
22. Z. Wang, W. Liu, W. He, H. Guo, L. Long, Y. Xi, X. Wang, A. Liu and C. Hu, *Joule*, 2021, 5, 441-455.
23. Y. Yu, Q. Gao, X. Zhang, D. Zhao, X. Xia, J. Wang, H. Li, Z. L. Wang and T. Cheng, *Energy & Environmental Science*, 2023, 16, 3932-3941.
24. K. Xia, J. Fu and Z. Xu, *Advanced Energy Materials*, 2020, 10.
25. Y. Xi, J. Wang, Y. Zi, X. Li, C. Han, X. Cao, C. Hu and Z. Wang, *Nano Energy*, 2017, 38, 101-108.